Ukrainian Journal of Remote Sensing
journal homepage: www.ujrs.org.ua

https://doi.org/10.36023/ujrs.2025.12.4.293

УДК 004.8:528.8:621.396.96

Predicting Filtered Image Quality Using Transfer Learning on Sentinel-1 Speckle Noise with DenseNet-121

R. Al-Senaikh* https://orcid.org/0000-0002-8059-4237
O. Rubel https://orcid.org/0000-0001-6206-3988

National Aerospace University "Kharkiv Aviation Institute", Vadyma Manka str., 17, Kharkiv, 61000, Ukraine

Speckle noise inherent to synthetic aperture radar (SAR) imagery degrades image quality and complicates automated analysis in Earth observation applications. Quantitative assessment of despeckling results requires computing quality metrics against reference images, which are unavailable in operational SAR scenarios. This paper presents a method for a priori prediction of filtered Sentinel-1 SAR image quality metrics before applying speckle noise filters. Unlike existing approaches predicting relative quality improvement, the proposed method predicts absolute values of five metrics (PSNR, WSNR, SSIM, MS-SSIM, FSIM) for a specific filter, enabling direct comparison and rational filter selection. The methodology employs transfer learning of DenseNet-121 convolutional neural network, pre-trained on ImageNet, adapted for single-channel SAR inputs through architectural modifications including input layer transformation, pooling optimization, and regression head replacement. A novel synthetic data generation pipeline utilizes histogram matching of Sentinel-2 optical images with Sentinel-1 SAR references to create training samples preserving ground truth. Dynamic gamma-distributed speckle noise addition with variable ENL $\in$ [2, 6] enhances data variability and model robustness. Experiments with six classical filters (Gamma MAP, Lee, Enhanced Lee, Frost, SRAD, Kuan) demonstrate high prediction accuracy across all filter-metric combinations. The coefficient of determination R^2 reaches 0.997 for best combinations and exceeds 0.97 for most of the 30 trained models. Mean absolute prediction errors remain below 0.29 dB for PSNR and 0.014 for SSIM across all tested configurations. The approach enables a priori quality prediction without reference images, allowing optimization of SAR processing workflows and resource planning before resource-intensive despeckling.

Keywords: Speckle noise, Sentinel-1, image quality metrics, DenseNet-121, transfer learning.

Introduction

Synthetic aperture radar (SAR) images are widely used in remote sensing applications; however, their quality is often degraded by multiplicative speckle noise, which complicates scene interpretation and automated analysis. Existing approaches to image quality assessment predominantly rely on statistical methods and require reference images, which are typically unavailable in practical SAR scenarios.

A priori assessment of expected quality after filtering is critical for rational selection of processing methods and reducing computational load in production SAR data processing pipelines. Such assessment enables exclusion of unpromising scenes, reduces error risk, and allows computation planning before launching resource-intensive procedures. In operational contexts, this capability supports several practical scenarios: automated filter selection in batch processing systems, where different scenes may benefit from different filtering approaches; resource allocation optimization in cloud-based SAR processing platforms; quality-driven prioritization of scene processing order; and early identification of scenes requiring special treatment or manual intervention.

The objective of this work is to develop a method for a priori prediction of absolute quality metric values (PSNR, WSNR, SSIM, MS-SSIM, FSIM) for filtered Sentinel-1 SAR scenes before applying speckle noise filters.

The novelty lies in applying transfer learning of a neural network to predict final, rather than incremental, quality metric values of filtered SAR images. Unlike existing approaches, the method does not require reference images and does not rely on calculating a predefined set of statistical features; relevant features are extracted automatically from input images. To enhance training data variability, dynamic addition of gamma-distributed speckle noise is employed.

*Corresponding author / Автор для кореспонденції: R. Al-Senaikh / Р.Ж. Аль-Сенайх / r.z.alsenaikh@khai.edu

The following notations are adopted in this work: S1-SAR denotes Sentinel-1 images (SAR, IW GRD, VV); S2-NIR denotes Sentinel-2 optical images (L2A, B8, 10 m). All derived versions (after p98-clipped max normalization, histogram matching, speckle addition/filtering) are denoted with the same prefixes.

Related Work

Classical methods for speckle noise suppression in SAR images include Gamma MAP (Medeiros et al., 2003; Sveinsson & Benediktsson, 1996; Beauchemin et al., 1996), Lee (Lee, 1980), Enhanced Lee, Frost (Frost et al., 1982), anisotropic diffusion SRAD (Yu & Acton, 2002), and Kuan (Kuan et al., 1985) filters. These approaches use local statistics and probabilistic models to achieve a balance between noise suppression and preservation of structural details.

Filtering quality is traditionally evaluated using PSNR, WSNR, SSIM, MS-SSIM, and FSIM metrics (Wang et al., 2004). Selection of the optimal filter is complicated by the dependence of results on scene characteristics and algorithm parameters.

To reduce computational costs, methods for a priori prediction of filter effectiveness have been proposed. Similar ideas for additive noise were developed in (Abramov et al., 2013; Lukin et al., 2014). For SAR data, approaches to predicting the effectiveness of Lee-like filters based on statistical features have been proposed, focusing on predicting the improvement in quality metrics (Rubel et al., 2015, 2019, 2020, 2021).

In parallel, image quality assessment methods are developing: full-reference (FR-IQA) and no-reference (NR-IQA). Modern NR-IQA models based on deep learning demonstrate high correlation with subjective assessment (IEEE, 2022; Talebi & Milanfar, 2018), but are oriented toward general visual quality.

Thus, a gap remains in the literature: there are no methods for a priori prediction of specific quality metrics for a given SAR filter.

Methodology

The developed methodology includes adaptation of the DenseNet-121 architecture for processing single-channel SAR images and creation of a synthetic data generation pipeline through histogram matching of Sentinel-2 optical images with reference Sentinel-1 SAR images.

Model Architecture and Transfer Learning

The proposed model is based on the DenseNet-121 network, pre-trained on the ImageNet dataset. To adapt it to single-channel SAR images, several modifications were made:

• The input Conv2d layer was changed from format (3, 64, 7×7) to (1, 64, 7×7) with weight averaging across channels. This approach preserves the learned filter responses by combining RGB channel weights into a single grayscale-equivalent filter, which is a standard technique for adapting pre-trained models to single-channel inputs.

• MaxPool was replaced with AvgPool for better preservation of texture characteristics (Wei et al., 2022).

• The classification head was replaced with a regression layer Linear(1024, 1).

A full fine-tuning strategy is applied, where all layers of the network, including Dense blocks and BatchNorm layers, are trained jointly. This ensures adaptation of the model to SAR data specifics and the quality metric prediction task.

Transfer learning enables utilization of universal features extracted from ImageNet, ensuring fast convergence when working with limited SAR scene datasets.

Table 1 presents a detailed comparison of the original DenseNet-121 architecture and the modified version for processing single-channel satellite images.

Table 1. DenseNet-121 modification for SAR filtering quality prediction

Parameter	Original (ImageNet)	Modified (S1-SAR)
Size	224×224	1024×1024
Channels	3 (RGB)	1 (grayscale)
Type	Photo	SAR
Tensor	[b,3,224,224]	[b,1,1024,1024]
Conv	Conv2d(3,64,7,2,3)	Conv2d(1,64,7,2,3)
Bias	True	False
Pool	MaxPool2d(3,2,1)	AvgPool2d(3,2,1)
Output	[b,64,56,56]	[b,64,256,256]
DB1 input	[b,64,56,56]	[b,64,256,256]
DB1 output	[b,256,56,56]	[b,256,256,256]
TL1	[b,128,28,28]	[b,128,128,128]
DB2 input	[b,128,28,28]	[b,128,128,128]
DB2 output	[b,512,28,28]	[b,512,128,128]
TL2	[b,256,14,14]	[b,256,64,64]
DB3 input	[b,256,14,14]	[b,256,64,64]
DB3 output	[b,1024,14,14]	[b,1024,64,64]
TL3	[b,512,7,7]	[b,512,32,32]
DB4 input	[b,512,7,7]	[b,512,32,32]
DB4 output	[b,1024,7,7]	[b,1024,32,32]
GAP input	[b,1024,7,7]	[b,1024,32,32]
GAP output	[b,1024]	[b,1024]
Linear in	1024	1024
Linear out	1000	1
Task	Classification	Regression

Synthetic Data Generation

Reference Sentinel-1 SAR Data

To create a statistical reference, denoised Sentinel-1 IW GRD images (VV polarization) are used. p98-clipped max normalization and Lee filtering (window 7×7) are applied to obtain a realistic amplitude distribution without pronounced speckle. Sentinel-1 GRD products are ready-to-use data with applied corrections and reduced speckle noise due to multi-look processing (Filipponi, 2019).

Sentinel-1 GRD products store pixel values in the amplitude domain, not intensities. The digital number (DN) for each pixel is calculated as shown in Equation 1 (European Space Agency, 2022):

$$DN = \text{round}\left(\sqrt{\frac{1}{N}\sum_{i=1}^{N}|s_i|^2} \times S \right). \quad (1)$$

where N is the number of looks (5×1 for IW GRD HR according to the official Sentinel-1 specification (European Space Agency, 2016)), s_i is the complex signal of the i-th look, S is the scaling factor from the Application LUT, depending on application and range, calculated as S_i = interpolate (θ_i), where θ_i is the incidence angle for pixel i. Note that N = 5 in the formula corresponds to the geometric number of looks, while ENL = 4.4 (European Space Agency, 2016) characterizes speckle suppression effectiveness accounting for correlations between neighboring pixels. In this study, we utilize Sentinel-1 Level-1 GRD products directly without radiometric calibration to sigma nought (σ^0). The pixel values represent detected amplitude (Digital Numbers), which preserve the image geometry and noise statistics required for the proposed learning-based filtering quality prediction approach. Since the quality metrics (PSNR, SSIM, etc.) are computed from relative intensity relationships rather than absolute physical values, the use of DN is sufficient for this task.

Sentinel-2 Optical Data

Optical images from Sentinel-2 Level-2A (B8 channel, 10 m resolution) are used, which do not contain speckle noise. The data undergo p98-clipped max normalization to match the dynamic range with SAR images.

The rationale for using optical imagery as the basis for synthetic ground truth is as follows: optical images provide clean geometric structure without speckle contamination, serving as ideal reference images for quality metric computation. While the physical mechanisms of optical reflectance and radar backscattering differ fundamentally, the proposed approach focuses on learning the relationship between image texture patterns and filtering quality metrics, rather than modeling radar physics. Histogram matching subsequently aligns the radiometric distribution of optical images with SAR statistics, creating training samples that are statistically representative of SAR imagery while preserving the known ground truth structure. This methodology enables controlled generation of noisy-clean image pairs essential for supervised learning of quality prediction.

Data Integration Process

Preprocessed S2-NIR and S1-SAR images are characterized by statistical features of mean brightness mu and standard deviation sigma. SAR scenes are clustered by their features using the k-means algorithm. The optimal number of clusters was determined using the Calinski-Harabasz (CH) Index, which evaluates the ratio of between-cluster to within-cluster variance. Analysis across k in [2, 60] revealed that while the global maximum is achieved at k = 2 (CH = 56.27), such coarse partitioning is insufficient for capturing the diverse scene semantics required for effective histogram matching. In the range k in [50, 60], the CH scores stabilize (22.04–24.38). The value k = 56 was selected as a local optimum (CH = 23.39) that exceeds the range mean (22.95). Crucially, this choice represents a trade-off that ensures sufficient semantic granularity of scene types while maintaining a constraint of at least 20 images per cluster, which is necessary for representative statistical sampling in the synthetic data generation pipeline. For each cluster, an equal (as far as possible) number of optical images S2-NIR is selected according to the minimum Euclidean distance criterion. Within the cluster, for each S2-NIR image, a corresponding S1-SAR reference image is randomly selected, further increasing scene diversity. The final stage includes histogram matching of optical images with paired SAR references.

The process of stylizing optical images into SAR-like images is illustrated in Fig. 1.

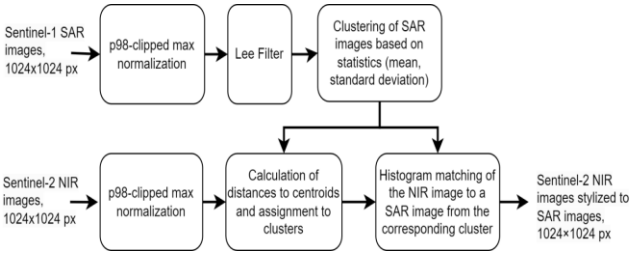

Fig. 1. Scheme of the process for stylizing S2-NIR optical images into SAR-like images. The process includes sequential transformation stages: from original optical images through normalization and clustering to final histogram matching with S1-SAR references

Histogram Matching Details

For histogram matching, for each optical image $I(x, y)$, an S1-SAR reference $R(x, y)$ from the same cluster is selected and a monotonic transformation (Equation 2) is applied:

$$I'_{hm}(x,y) = F_R^{-1}(F_I(I(x,y))), \quad (2)$$

where (x, y) are pixel coordinates in the image, F_I, F_R are empirical cumulative distribution functions (CDF) of brightness for the original and reference images, respectively. This monotonic transformation is based on the principle of preserving rank relationships between pixels. The function $F_I(I(x, y))$ transforms the pixel brightness into its percentile in the original image, while $F_R^{-1}(\cdot)$ finds the corresponding brightness value in the reference image for the same percentile. Histogram matching is a pixel-wise (pointwise) operation that modifies only intensity values without altering spatial positions of pixels; consequently, the geometric structure of the original image remains unchanged. The preservation of rank order ensures that local contrast relationships are maintained after the transformation.

The correctness of histogram matching is demonstrated in Fig. 2, which shows KDE curves (Kernel Density Estimation – a non-parametric method for density estimation) of brightness for the denoised S1-SAR image, stylized optical, and original optical images. KDE provides a smooth estimation of data density distribution, allowing visual comparison of statistical characteristics of images. The green and red lines practically coincide, indicating distribution matching after histogram matching, while the blue line illustrates the original S2-NIR statistics.

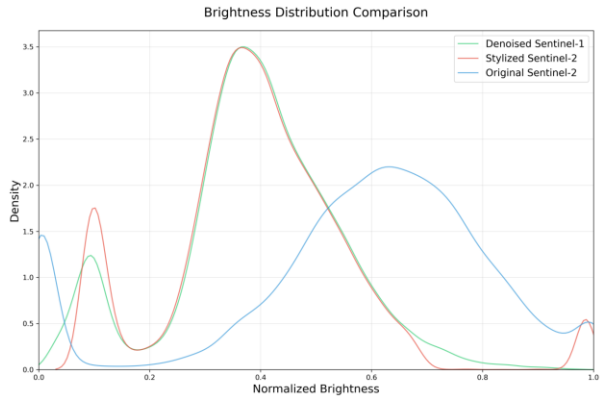

Fig. 2. Comparison of brightness distributions for images (fragments shown in Fig. 3): denoised S1-SAR (b, green line), stylized S2-NIR after histogram matching (e, red line), and original S2-NIR (c, blue line).

The effectiveness of the stylization procedure is demonstrated by comparative analysis of six fragments in Fig. 3. Visually, it can be observed that the stylized noisy fragment (f) shows greater photometric similarity to the original SAR fragment (a) compared to the simply noised optical fragment (d).

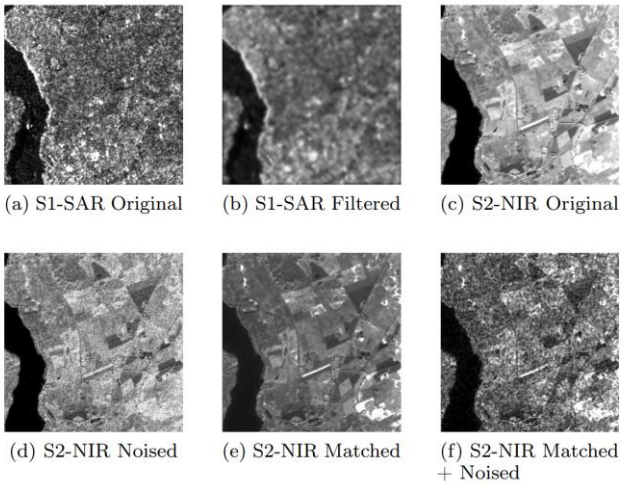

Fig. 3. Comparison of S1-SAR and S2-NIR fragments at different processing stages: (a) S1-SAR original, (b) S1-SAR after Lee filtering, (c) S2-NIR original, (d) S2-NIR noised, (e) S2-NIR after histogram matching, (f) S2-NIR stylized noised

The final synthetic S2-NIR dataset reproduces the radiometric characteristics of S1-SAR images while preserving the geometric structure of optical images, providing an appropriate basis for training the DenseNet-121 model.

Dynamic Speckle Noise Addition

During training, each stylized optical image receives a new realization of multiplicative speckle noise with random parameters corresponding to Sentinel-1 SAR image characteristics. Dynamic noise addition in each epoch significantly increases data variability and eliminates the need to store numerous image copies while maintaining experiment reproducibility.

Speckle noise model and parameterization

The work uses a multiplicative speckle model in *intensities* (Equation 3):

$$Y(x, y) = X(x, y) \cdot S(x, y), \quad S \sim \Gamma(k = L, \theta = 1/L), \quad (3)$$

Where X is the true scene intensity, Y is the observed intensity, S is the speckle multiplier, and $L \equiv \mathrm{ENL}$ (equivalent number of looks).

This parameterization of the gamma distribution ensures $\mu_s = 1$ (mean speckle value) and $\sigma_s^2 = 1/L$ (speckle variance), which corresponds to the physical properties of speckle. The coefficient of variation CV (coefficient of variation), characterizing the relative noise variability, is determined as shown in Equation 4:

$$\mathrm{CV}^2 = \frac{\sigma_s^2}{\mu_s^2} = \frac{1/L}{1^2} = \frac{1}{L}, \ \mathrm{CV} = \frac{1}{\sqrt{L}}. \quad (4)$$

Experiments used values $L \in [2, 6]$ characteristic of Sentinel-1 IW GRD, which is consistent with classical speckle models (Lee, 1980; Frost et al., 1982; Medeiros et al., 2003; Singh & Pandey, 2016; Moein & Taban, 2024) and Sentinel-1 GRD preprocessing methods (Filipponi, 2019). Dynamic addition of speckle noise with random ENL values in the specified range ensures training of a model robust to different noise levels.

Implementation details (low-frequency texture and upsampling)

Noising of stylized images is performed in the intensity domain to ensure physical correctness of the speckle model. The process includes conversion from amplitude representation to intensities, generation of gamma-distributed speckle noise at reduced resolution to create large-scale texture variations, upsampling the noise to original resolution, multiplicative noise application, and conversion back to amplitude domain followed by normalization. These stages are integrated into the general quality assessment scheme shown in Fig. 4.

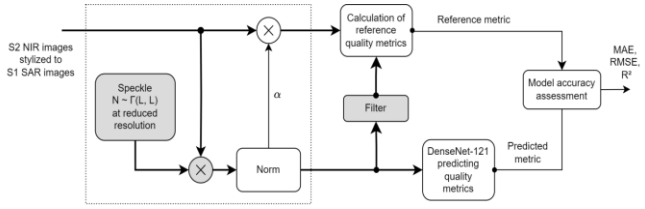

Fig. 4. Validation scheme: comparison of model predictions with real filtering results. Gray blocks denote processing stages in the intensity domain

To control the speckle correlation length, a scale $s \in (0,1]$ (Lee, 1980) is u sed: smaller values of s lead to a larger correlation length (increased spatial correlation), while larger values of s lead to a finer one. Let the original image have size $H \times W$. A low-resolution noise map of size is constructed according to Equation 5:

$$H_s = \lfloor sH \rfloor,\ W_s = \lfloor sW \rfloor. \quad (5)$$

On this grid, speckle is independently sampled:

$$S_{\downarrow}(i,j) \sim \Gamma(k = L, \theta = 1/L), \quad (5a)$$

$$(i,j) \in \{1,...,H_s\} \times \{1,...,W_s\}. \quad (5b)$$

Next, bilinear upsampling to the original size is performed (Equation 6):

$$\tilde{S} = U_{bilinear}(S_{\downarrow}; H, W). \quad (6)$$

To preserve the statistics of the gamma map after upsampling, renormalization is applied. First, the statistics are calculated (Equations 7 and 8):

$$\mu_{s,\downarrow} = \text{mean}(S_{\downarrow}),\ \sigma_{s,\downarrow} = \text{std}(S_{\downarrow}), \quad (7)$$

$$\mu_{s,\sim} = \text{mean}(\tilde{S}),\ \ \sigma_{s,\sim} = \text{std}(\tilde{S}), \quad (8)$$

and the final multiplier is formed according to Equation 9:

$$S = \frac{\tilde{S} - \mu_{s,\sim}}{\sigma_{s,\sim}} \sigma_{s,\downarrow} + \mu_{s,\downarrow}. \quad (9)$$

The noisy image is obtained by applying multiplicative noise according to Equation 10:

$$Y = X \odot S. \quad (10)$$

The optimal value $s = 0.6$ was determined empirically based on analysis of the autocorrelation function (ACF) of reference SAR images and experiments with varying s (0.2, 0.4, 0.6, 0.8, 1.0). Detailed ACF analysis for different values of s is presented in the supplementary materials to the article. The selected value minimizes the discrepancy between ACF of synthetic and real Sentinel-1 data, ensuring visual similarity of synthetic noisy images to real ones.

This approach ensures generation of images that are radiometrically and in terms of noise characteristics statistically equivalent to real Sentinel-1 SAR data, while preserving the geometric structure of the original optical images.

Normalization of noisy images

The final stage of the noising process is normalization of the noisy images (see Fig. 4) to eliminate dependence of predictions on radiometric image characteristics. This is critically important for correct model training, since without normalization the model might learn to predict filtering quality based on simple brightness analysis rather than complex texture and structural image characteristics.

Normalization is performed by dividing each noisy image by its mean value (Equation 11):

$$I_{\text{noisy\_norm}} = \frac{I_{\text{noisy}}}{\mu_{I_{\text{noisy}}}}, \quad (11)$$

where $\mu_{I\text{noisy}}$ is the mean brightness value of the noisy image. Accordingly, clean (reference) images are normalized by the same coefficient (Equation 12):

$$I_{\text{clean\_norm}} = \frac{I_{\text{clean}}}{\mu_{I_{\text{noisy}}}}. \quad (12)$$

Such normalization ensures that all images have unit mean brightness value, which eliminates the possibility for the model to use radiometric characteristics as an indicator of noise level. The model is forced to analyze more complex spatial patterns and texture features for a priori prediction of filtered image quality, which increases its generalization ability and robustness to lighting variations and scene radiometric characteristics.

Experimental Setup

Data Splitting

The synthetic dataset (1910 stylized S2-NIR images) was split in an 80/20 ratio into training (1528 images) and test (382 images) sets. S1-SAR images (1522 images) were used only as references for histogram matching.

Models were trained on the training set with validation on the test set. Final evaluation was performed on models with the best results on training data to ensure correct assessment of generalization ability.

Ground Truth Generation and Quality Metrics

Data Processing Domains

Data processing is performed in domains aligned with signal physics and target product format. The Sentinel-1 IW GRD product is published in the amplitude domain (DN proportional to echo-signal root-mean-square amplitude) (European Space Agency, 2022), and it is this product that undergoes filtering and visual assessment. Accordingly, references and target quality metrics (PSNR, WSNR, SSIM, MS-SSIM, FSIM) are calculated in the amplitude domain: this ensures metric comparability with GRD images, correct result interpretability, and consistency with visual perception (Wang et al., 2004). In contrast, speckle noise modeling and suppression are performed in the intensity domain, where the standard multiplicative model $Y = X \cdot S$ holds with gamma-distributed multiplier at $L \equiv \text{ENL}$. For data synthesis and application of classical filters, the image is converted from amplitude to intensity (by squaring), noising and filtering are performed, after which the result is returned to the amplitude domain for assessment. This decomposition of stages simultaneously preserves physical correctness of the noise model in intensities and ensures that the final quality assessment is conducted in the same domain as the original GRD product, providing direct visual comparability with the original amplitude image.

Procedure for Generating Ground Truth Metric Values

Ground truth metric values are formed as follows: multiplicative speckle noise is added to stylized optical images (in the amplitude domain), for which the data is converted to the intensity domain (by squaring), where a gamma-distributed multiplier is applied, after which the result is converted back to the amplitude domain. The

resulting noisy images are then filtered using one of the investigated methods in the intensity domain. Ground truth metric values are calculated by comparing the filtered images (in the amplitude domain) with the original stylized images without noise. The model is trained to predict expected quality metric values based on noisy images in the amplitude domain, which ensures correspondence with human image perception.

Model Performance Metrics

Three metrics were used to assess the quality of model predictions, which measure the accuracy of predicting target image quality metric values:

Mean Absolute Error (MAE) (Equation 13):

$$MAE = \frac{1}{N}\sum_{i=1}^{N}|y_i - \hat{y}_1|, \quad (13)$$

where y_i are the true quality metric values, $\hat{y}_i$ are the values predicted by the model, N is the number of observations.

Root Mean Square Error (RMSE) (Equation 14):

$$RMSE = \sqrt{\frac{1}{N}\sum_{i=1}^{N}(y_i - \hat{y}_i)^2}. \quad (14)$$

Sensitive to large prediction errors.

Coefficient of Determination (R^2) (Equation 15):

$$R^2 = 1 - \frac{\sum_{i=1}^{N}(y_i - \hat{y}_i)^2}{\sum_{i=1}^{N}(y_i - \bar{y})^2}, \quad (15)$$

where $\bar{y}$ is the mean value across all true y_i values. Characterizes the fraction of variance explained by the model (higher = better).

Image Quality Metrics

The following are the image quality metrics that the model predicts for each filter type. These metrics assess the quality of filtered images relative to reference (noise-free) images:

The PSNR (Peak Signal-to-Noise Ratio) metric measures the ratio of the maximum possible signal value to noise power (Equation 16):

$$PSNR = 20\log_{10}\left(\frac{MAX_I}{\sqrt{MSE}}\right), \quad (16)$$

where $MSE = \frac{1}{HWC}\sum(I_{\text{denoised}} - I_{\text{clean}})^2$ is the mean square error across all pixels, channels, and spatial dimensions, MAX_I is the maximum intensity value (usually 1.0 for normalized images). Units: dB (higher = better).

The WSNR (Weighted Signal-to-Noise Ratio) metric is calculated in the frequency domain using the Contrast Sensitivity Function (CSF) for weighting different frequency components (Equation 17):

$$WSNR = 10\log_{10}\left[\frac{\sum_{c,h,w}|S_{c,h,w}|^2 \times W_{h,w}}{\sum_{c,h,w}|N_{c,h,w}|^2 \times W_{h,w}}\right], \quad (17)$$

where $S_{c,h,w}$ are the spectral components of the original image, $N_{c,h,w}$ are the spectral components of noise (difference between original and processed image), $W_{h,w}$ is the CSF weighting function for spatial frequencies. Units: dB (higher = better).

The SSIM (Structural Similarity Index Measure) metric assesses structural similarity between two images by analyzing brightness, contrast, and structure (Equation 18):

$$SSIM(x,y) = \frac{(2\mu_x\mu_y + C_1)(2\sigma_{xy} + C_2)}{(\mu_x^2 + \mu_y^2 + C_1)(\sigma_x^2 + \sigma_y^2 + C_2)}, \quad (18)$$

where μ_x, μ_y are the mean brightness values of images x and y, σ_x^2, σ_y^2 are variances (contrast), σ_{xy} is covariance between x and y (structure), $C_1 = 0.01^2 = 0.0001$, $C_2 = 0.03^2 = 0.0009$ are stabilization constants for images in range [0, 1]. Value range: [–1,1] (where 1 means perfect match).

The MS-SSIM (Multi-Scale Structural Similarity Index) metric is calculated as weighted product of SSIM at different scales (Equation 19):

$$MS\text{-}SSIM(x,y) = \prod_{j=0}^{4}[SSIM(x_j, y_j)]^{w_j}, \quad (19)$$

where x_j, y_j are images at scale j after downsampling (starting from original size), w_j are weighting coefficients with values $w_0 = 0.0448$, $w_1 = 0.2856$, $w_2 = 0.3001$, $w_3 = 0.2363$. Each subsequent image is reduced by 2 times using average pooling. Value range: [0,1] (where 1 means perfect match).

The FSIM (Feature Similarity Index) metric uses phase and gradient information in feature space (Zhang et al., 2011) (Equation 20):

$$FSIM = \sum\frac{(PC_m \times SC_m) \times (PC_n \times SC_n)}{(PC_m \times SC_m) + (PC_n \times SC_n)}, \quad (20)$$

where PC_m (Phase Congruency) is phase congruency, SC_m (Similarity of Gradient) is gradient similarity, and indices m and n denote two similarity measures. Value range: [0,1] (where 1 means perfect match).

Training Settings

Models were trained in PyTorch using NVIDIA RTX 4090 GPU. Hyperparameters:

- Optimizer: Adam ($\eta = 10^{-4}$)
- Epochs: 120
- Batch size: 4 images (1024×1024)
- Loss function: MSE
- Gradient accumulation: 2 steps

For each combination of filter (6 types) and quality metric (5 types), independent training was conducted with dynamic speckle noise addition (ENL ∈ [2,6]).

Epoch duration varied from 43 to 210 seconds depending on the filter-metric combination. Total training time for all 30 experiments was approximately 60 hours. Full fine-tuning strategy of DenseNet-121 was applied.

Evaluation Methodology

Model prediction accuracy assessment (Fig. 4) is based on comparing its output values with ground truth. Ground truth metrics are formed by adding speckle noise to stylized images, followed by filtering and calculation of

quality metrics relative to original clean images. Simultaneously, the same noisy images are fed to the model to obtain predictions. The accuracy of the final comparison is assessed using MAE, RMSE, and R^2.

Reproducibility and Availability

Data. Original Sentinel-1 (IW GRD) and Sentinel-2 (L2A) scenes were obtained from the Copernicus Data Space Ecosystem platform. Sentinel-2 data were segmented into 1024×1024 pixel patches with histogram matching of optical images to SAR radiometry. The processed dataset is hosted in the Zenodo repository: https://zenodo.org/uploads/17253925. After publication, a permanent DOI will be obtained for citation.

Code. Python implementation is available in the GitHub repository: https://github.com/rsenaikh/Predicting_Quality_after_Noise_Removal with reproduction instructions.

Experiments. All experiments were conducted on NVIDIA RTX 4090 GPU using PyTorch and NumPy. Detailed training settings are provided in Section 4.

Ethics. Sentinel-1/2 data are distributed under open Copernicus license. Ethical approvals are not required.

Results and Discussion

Training Dynamics

The training curves (Fig. 5) demonstrate two key phases. The sharp initial error reduction is explained by effective transfer of low-level texture features from the ImageNet pre-trained model (Wanjiku et al., 2022), where universal features (edges, textures) ensure fast convergence in early stages, minimizing the need for additional regularization. This is followed by a phase of asymptotic approach to values on the order of 10^{-5}, with synchronous dynamics of training and test curves without divergence indicating absence of overfitting. This behavior confirms the effectiveness of the full fine-tuning strategy, where all layers, including Dense blocks and BatchNorm layers, are adapted jointly, ensuring comprehensive tuning to SAR data specifics and the regression task.

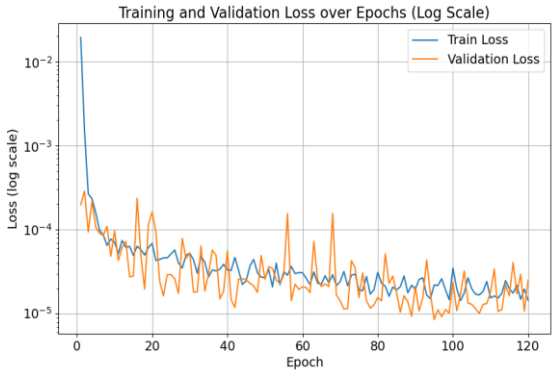

Fig. 5. Model training dynamics (Kuan filter, WSNR metric): loss function on training and test sets

Qualitative Examples

Fig. 6 shows model predictions for a fragment processed with Lee and Gamma MAP filters. The predicted values demonstrate high accuracy with absolute errors of 0.036 dB and 0.037 dB respectively, illustrating the feasibility of the proposed approach for a priori prediction of filtered image quality.

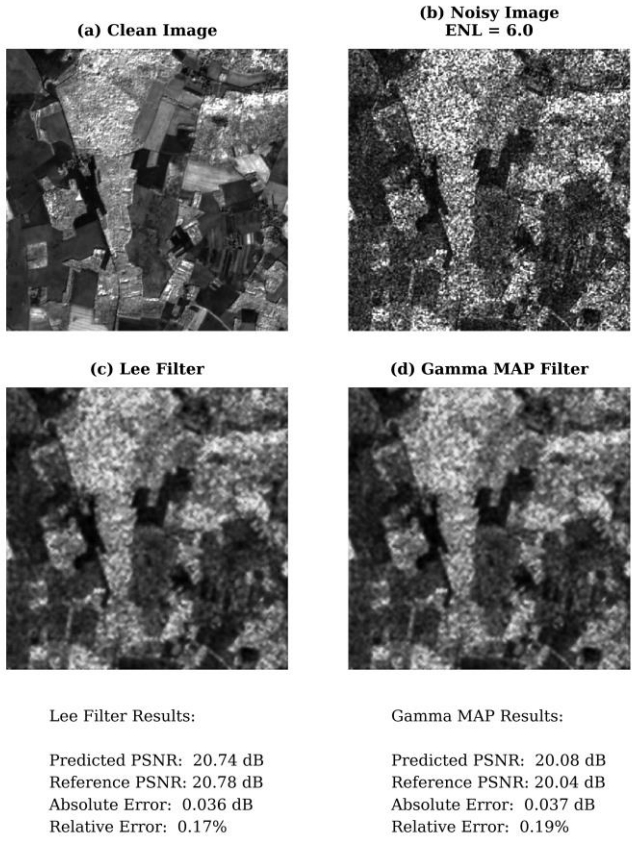

Fig. 6. Comparison of predicted and true PSNR values for Lee and Gamma MAP filters on test images. Shown are original noisy images, filtering results, and corresponding quality metric values

Quantitative Results

Table 2 contains MAE, RMSE, and R^2 values for all combinations of filters and quality metrics. All results are obtained on the test set of 382 stylized images sized 1024×1024 pixels.

Table 2. Prediction accuracy of filtering quality

Filter	Stat	PSNR	SSIM	MS-SSIM	FSIM	WSNR
Gamma Map	MAE	0.2884	0.0132	0.0054	0.0021	0.1402
	RMSE	0.4475	0.0222	0.0082	0.0027	0.1944
	R^2	0.9886	0.9693	0.9972	0.9826	0.9972
Lee	MAE	0.1077	0.0043	0.0023	0.0023	0.0459
	RMSE	0.1425	0.0058	0.0037	0.0037	0.0635
	R^2	0.9864	0.9777	0.9518	0.9546	0.9966
Enhanced Lee	MAE	0.0587	0.0064	0.0023	0.0025	0.0442
	RMSE	0.0803	0.0086	0.0031	0.0044	0.0575
	R^2	0.9957	0.9343	0.9605	0.9364	0.9965
Frost	MAE	0.0805	0.0040	0.0019	0.0025	0.1318
	RMSE	0.106	0.0054	0.0029	0.004	0.1822
	R^2	0.9949	0.9825	0.9756	0.9609	0.9911
Srad	MAE	0.2391	0.0053	0.0025	0.0025	0.2781
	RMSE	0.2964	0.0073	0.0038	0.0038	0.3582
	R^2	0.9523	0.9644	0.955	0.9577	0.9429

Kuan	MAE	0.0514	0.0039	0.0021	0.0027	0.0486
	RMSE	0.0722	0.0054	0.003	0.004	0.0637
	R^2	0.996	0.9812	0.9666	0.9519	0.9963

The average coefficient of determination R^2 across all filter-metric combinations is 0.9732 ± 0.0201.

Scatter plots (Fig. 7) show predicted and true values of quality metrics for selected filter-metric combinations.

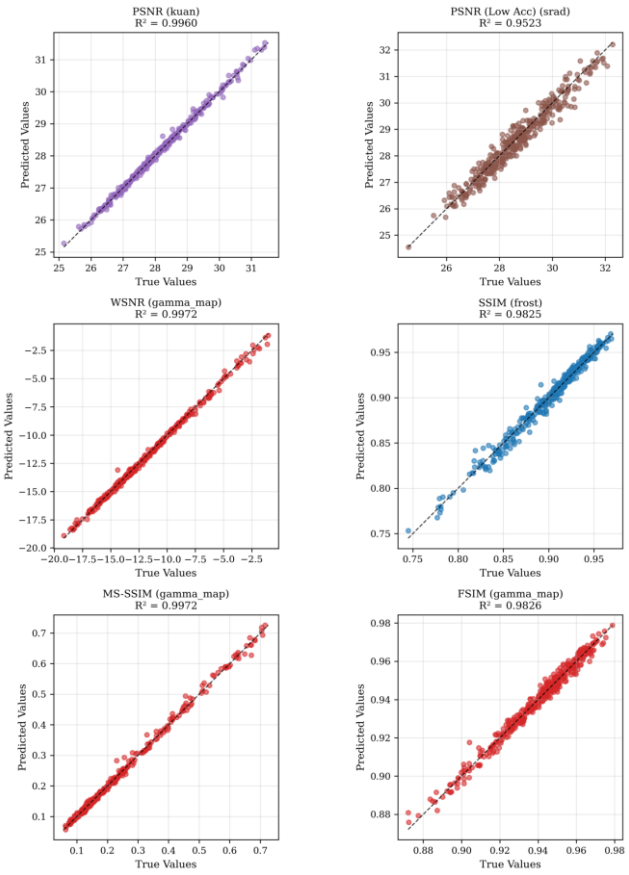

Fig. 7. Scatter plots of predicted vs. true values for selected quality metrics (PSNR, WSNR, SSIM, MS-SSIM, FSIM) with filters providing the best prediction accuracy.

Plots of normalized mean absolute error (NMAE) dependence on noise level (Fig. 8) show the change in prediction error depending on the equivalent number of looks (ENL) in the range [2, 6].

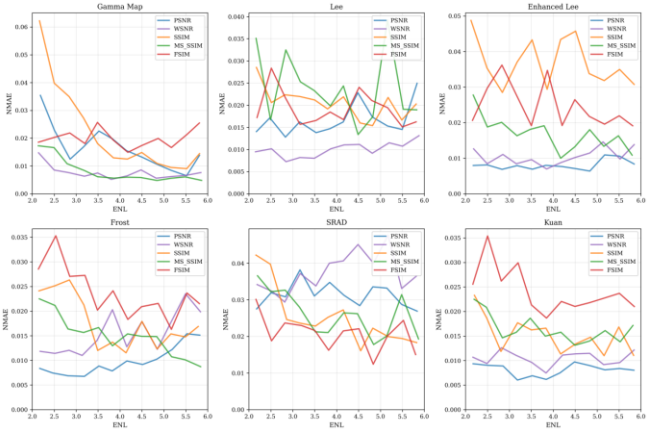

Fig. 8. Dependence of normalized prediction error on noise level (ENL)

Prediction error histograms (Fig. 9) show the distribution of errors for different filter-metric combinations.

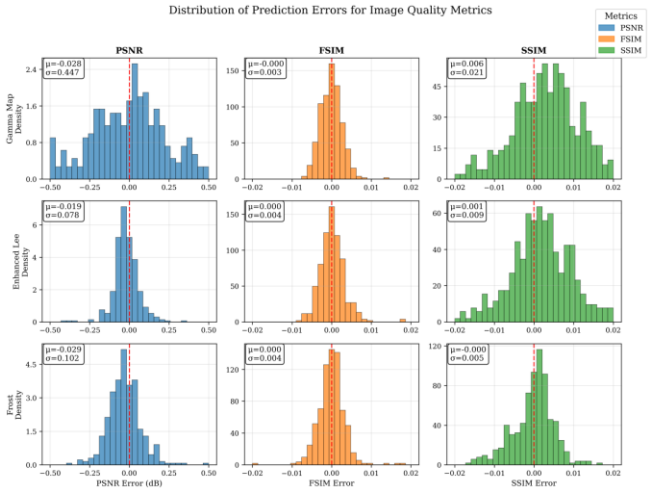

Fig. 9. Prediction error histograms for different filter-metric combinations

Results Analysis

The results show high values of the coefficient of determination R^2 for most filter-metric combinations ($R^2 > 0.97$ for most combinations). The maximum value $R^2 = 0.9972$ was achieved for MS-SSIM and WSNR metrics of the Gamma MAP filter. The minimum value $R^2 = 0.9343$ is observed for the SSIM metric and Enhanced Lee filter.

The aggregated distribution of values across all filter-metric pairs is shown in the heatmap (Fig. 10). The heatmap reveals distinct patterns: maximum values occur for noise-sensitive metrics (PSNR, WSNR), while structural metrics (SSIM, MS-SSIM, FSIM) exhibit lower R^2 values.

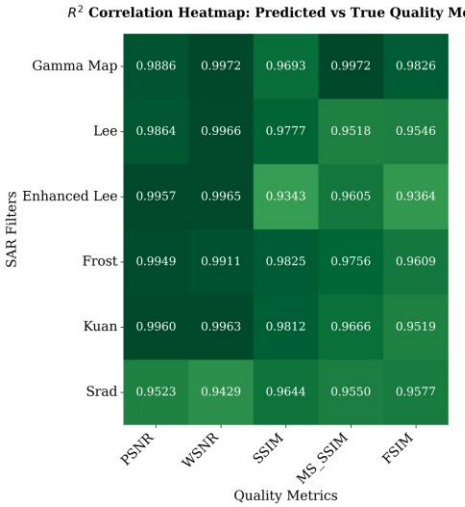

Fig. 10. Heatmap of coefficient of determination R^2 for different filters and quality metrics

Detailed results by quality metric types are shown in Table 3, presenting average R^2 values and ranges for each metric.

Table 3. Prediction accuracy analysis by quality metric types

Metric	Average R^2	Range
PSNR	0.987	[0.952, 0.996]
WSNR	0.987	[0.943, 0.997]
SSIM	0.968	[0.934, 0.982]
MS-SSIM	0.969	[0.952, 0.997]
FSIM	0.957	[0.937, 0.983]

Results breakdown by filter types is presented in Table 4, containing average R^2 values and ranges for each filter.

Table 4. Prediction accuracy analysis by filter types

Filter	Average R^2	Range
Gamma MAP	0.987	[0.969, 0.997]
Kuan	0.978	[0.952, 0.996]
Frost	0.978	[0.960, 0.995]
Enhanced Lee	0.963	[0.934, 0.997]
Lee	0.973	[0.952, 0.997]
SRAD	0.955	[0.943, 0.964]

At the filter level, the lowest R^2 values are observed for SRAD compared to other filters, which may be related to the specifics of anisotropic diffusion requiring more complex modeling of spatial gradients. In contrast, Kuan, Frost, and Enhanced Lee filters demonstrate high $R^2 > 0.99$ values for noise-sensitive metrics, explained by more predictable distortion patterns created by adaptive methods based on local scene statistics (Lee, 1980).

At the metric level, FSIM depends on phase congruency and texture features, going beyond amplitude and contrast distortions characteristic of PSNR/WSNR and partially SSIM/MS-SSIM (Wang et al., 2004). Accordingly, FSIM prediction proves most challenging, reflected in relatively lower R^2 values.

These patterns are consistent with DenseNet-121 properties. Feature concatenation within dense blocks preserves early maps containing local statistics (means, variances, texture patterns), supporting high R^2 for noise-sensitive PSNR/WSNR metrics. As the network deepens, receptive field increases, forming multi-scale representations that contribute to SSIM/MS-SSIM accuracy. Together, this explains high R^2 for most filters and relative difficulty in predicting SRAD, requiring precise modeling of anisotropic diffusion processes.

Scatter plots demonstrate nearly linear correspondence between predictions and true values with narrow dispersion across the entire metric range, indicating absence of bias and high model calibration.

NMAE dependence plots on ENL show weak sensitivity of error to speckle level in the [2, 6] interval and stability of estimates across samples, indicating robustness to noise variations.

Error histograms are approximated by normal distribution with zero mean and no pronounced asymmetry, ruling out systematic biases and confirming correct model specification.

Recommendations for Metric Selection

Based on the obtained results and metric characteristics, the following recommendations for metric selection depending on application context can be formulated:

• PSNR and WSNR are recommended for applications where overall noise suppression level is the primary concern, such as preliminary scene assessment or batch processing quality control. WSNR additionally accounts for human visual perception through frequency weighting.

• SSIM and MS-SSIM are preferable for tasks requiring preservation of structural information, such as change detection, object recognition, or visual interpretation. MS-SSIM provides more robust assessment across different scales and is recommended for heterogeneous scenes.

• FSIM is recommended for applications sensitive to fine texture and phase information, such as interferometric processing preparation or detailed terrain analysis. However, its prediction shows lower accuracy, suggesting careful validation for critical applications.

• For general-purpose filter selection, a combination of PSNR (noise assessment) and SSIM (structure preservation) provides a balanced evaluation approach.

Comparison with Baseline Methods

The proposed approach differs from existing statistical methods (Rubel et al., 2019, 2020, 2021) based on calculating 28 expert features. Direct quantitative comparison with these methods is difficult since they focus on predicting the *relative improvement* in quality metrics, while the proposed model predicts *absolute values*. Nevertheless, the fundamental advantage of deep learning lies in automatic extraction of hierarchical features, eliminating the need for labor-intensive manual design and ensuring higher generalization ability.

Key differences:

• End-to-end hierarchical feature extraction by deep neural network instead of manual design and calculation of fixed statistical characteristic set.

• Prediction of final absolute quality metric values rather than their relative improvement (gain), which is a more complex and practically significant task.

• Application of transfer learning based on DenseNet-121 deep convolutional network adapted for processing single-channel SAR images of high resolution (1024×1024 pixels).

• Unified and robust model capable of predicting quality for a specific filter and adapting to variable noise levels (ENL $\in$ [2,6]) without additional training.

• Use of innovative synthetic data generation pipeline based on histogram matching of optical (Sentinel-2) and SAR (Sentinel-1) references for creating photorealistic training samples.

• Application of complex speckle noise model with controlled spatial correlation and data normalization to

ensure prediction invariance to scene radiometric characteristics.

Results (R^2 = 0.9886 for PSNR of Gamma MAP filter, where PSNR is chosen as the most universal quality metric and Gamma MAP as one of the most effective adaptive filters) confirm the effectiveness of deep learning for a priori prediction of absolute quality metric values for SAR image filtering, which is a more complex and practically significant task compared to predicting relative improvement.

Limitations

Despite high results, the approach has limitations:

• Synthetic nature of data limits generalizability to real SAR scenes with geometric distortions (layover, shadow, foreshortening), requiring additional validation on real data.

• Fixed image size (1024×1024 pixels) limits applicability to scenes of arbitrary size.

• Noise range is limited to typical Sentinel-1 IW GRD conditions (ENL ∈ [2,6]), which may reduce accuracy for other SAR systems.

• Synthetic nature of data based on Sentinel-2 optical images does not account for SAR-specific geometric distortions (*layover*, *shadow*, *foreshortening*) inherent to complex terrains. This is a key limitation requiring additional validation on real SAR data containing such artifacts to assess model generalization ability.

• The physical mechanisms of optical reflectance and radar backscattering differ fundamentally. While histogram matching aligns statistical distributions, it cannot fully replicate the scattering behavior of different surface types in SAR imagery. This may affect model performance on scenes where optical-radar contrast relationships differ significantly from the training data.

• Potential contrast inversion between optical and radar images (e.g., water bodies appearing bright in optical but dark in SAR, or urban areas with different backscattering characteristics) represents an unexplored factor that may influence stylization quality and subsequent prediction accuracy.

• The study focuses exclusively on VV polarization; applicability to VH polarization and cross-polarization scenarios remains to be validated.

Future Perspectives and Research

The obtained results open several directions for further development:

• **Real Data Validation:** Extension of research to real Sentinel-1 SAR scenes with geometric distortions (layover, shadow, foreshortening) to assess model generalizability.

• **Noise Range Extension:** Model adaptation for operation with extreme noise levels (ENL < 2 and ENL > 6) characteristic of other SAR systems (ALOS PALSAR, TerraSAR-X).

• **Multispectral Data:** Extension of approach to complex SAR images and polarimetric data for a priori prediction of filtered image quality in different polarization channels.

• **Adaptive Architectures:** Investigation of attention mechanisms and transformer architectures to improve prediction accuracy for complex metrics like FSIM.

• **Pipeline Integration:** Implementation of the model in operational SAR data processing chains for automatic selection of optimal filtering parameters.

• **Radiometric Calibration:** While this study demonstrates effectiveness on GRD data with DN values, future implementations intended for physical parameter retrieval should investigate the impact of radiometric calibration (conversion to σ^0 or γ^0) on prediction accuracy.

• **Polarization Diversity:** Validation of the approach on VH polarization data and investigation of cross-polarization scenarios to extend applicability to dual-polarization Sentinel-1 products.

• **Pipeline Performance Evaluation:** Theoretical and experimental assessment of end-to-end processing pipeline performance, including computational efficiency analysis and comparison with direct filtering approaches in terms of time-quality trade-offs.

• **Contrast Inversion Analysis:** Systematic investigation of the impact of optical-radar contrast inversion on stylization quality and prediction accuracy across different land cover types.

Conclusion

A method for a priori prediction of filtered Sentinel-1 SAR image quality based on adapted DenseNet-121 has been developed. This approach predicts absolute values of quality metrics (PSNR, WSNR, SSIM, MS-SSIM, FSIM) for a specific filter before its application.

Experiments with six classical filters achieved high accuracy indicators: $R^2 \geq 0.97$ for most combinations (Table 2).

Key contributions:

• Formulation of the task of a priori prediction of specific quality metrics for a given filter.

• DenseNet-121 adaptation to single-channel SAR inputs with full fine-tuning.

• Synthetic data generation pipeline through histogram matching of optical and SAR images with dynamic speckle noise addition.

Solved tasks:

• Developed a physically consistent pipeline with processing in intensities (for noise and filtering) and assessment in amplitudes (for metrics), matching the Sentinel-1 GRD product format.

• Constructed a SAR-like synthetic dataset by histogram matching Sentinel-2 (B8) to Sentinel-1 references, with dynamic, spatially correlated speckle generation (ENL ∈ [2,6]) and per-image normalization.

• Adapted and fully fine-tuned DenseNet-121 for single-channel 1024×1024 inputs (modified stem/pooling and regression head) for metric value prediction.

• Generated ground-truth for six classical filters (Gamma MAP, Lee, Enhanced Lee, Frost, SRAD, Kuan)

across five metrics (PSNR, WSNR, SSIM, MS-SSIM, FSIM) and trained 30 specialized models.

• Demonstrated robustness to noise level variation and scene diversity, with near-linear calibration of predictions versus ground truth.

Quantitatively, the best results reached $R^2 = 0.997$ (Gamma MAP: MS-SSIM/WSNR), with an average across all filter–metric pairs of $R^2 = 0.9732 \pm 0.0201$ and low absolute errors (see Tables 2–4).

Practical implications:

• A priori ranking and selection of filters and their parameters without running expensive despeckling.

• Early scene triage and compute budgeting in operational SAR processing chains.

• Straightforward integration as a fast pre-filtering module; code and data are publicly available for reproduction and deployment.

This approach enables optimization of filter selection before performing resource-intensive computations, reducing costs and increasing SAR data processing efficiency.

Future research directions:

• Validation on real SAR scenes accounting for geometric distortions.

• Extension of noise parameter ranges and image sizes.

• Investigation of alternative architectures and multi-level inputs.

• Assessment of prediction uncertainty and joint filter ranking.

Contributions of Authors: Conceptualization – R. Al-Senaikh and O. Rubel; methodology – R. Al-Senaikh; formal analysis – R. Al-Senaikh; investigation – R. Al-Senaikh and O. Rubel; data curation – R. Al-Senaikh and O. Rubel; writing – original draft preparation – R. Al-Senaikh; writing – review and editing – R. Al-Senaikh and O. Rubel; visualization – R. Al-Senaikh. All authors have read and agreed to the published version of the manuscript.

Funding: This research received no external funding.

Data Availability Statement: The processed dataset is available in the Zenodo repository (https://zenodo.org/uploads/17253925). Python implementation code is available in the GitHub repository (https://github.com/rsenaikh/Predicting_Quality_after_Noise_Removal).

Acknowledgments: The authors would like to express their sincere gratitude to the Copernicus Data Space Ecosystem for providing open access to Sentinel-1 and Sentinel-2 data. We are also grateful to reviewers and editors for their valuable comments, recommendations, and attention to the work.

Conflicts of Interest: The authors declare no conflict of interest.

Внесок авторів: Концептуалізація – Р. Аль-Сенайх та О. Рубель; методологія – Р. Аль-Сенайх; формальний аналіз – Р. Аль-Сенайх; дослідження – Р. Аль-Сенайх та О. Рубель; обробка даних – Р. Аль-Сенайх та О. Рубель; написання – підготовка оригінального тексту – Р. Аль-Сенайх; написання – рецензування та редагування – Р. Аль-Сенайх та О. Рубель; візуалізація – Р. Аль-Сенайх. Всі автори прочитали та погодилися з опублікованою версією рукопису.

Фінансування: Це дослідження не отримало зовнішнього фінансування.

Доступність даних: Оброблений набір даних доступний у репозиторії Zenodo (https://zenodo.org/uploads/17253925). Код програмної реалізації на Python доступний у репозиторії GitHub (https://github.com/rsenaikh/Predicting_Quality_after_Noise_Removal).

Подяки: Автори висловлюють щиру подяку Copernicus Data Space Ecosystem за надання відкритого доступу до даних Sentinel-1 та Sentinel-2. Також вдячні рецензентам та редакторам за цінні коментарі, рекомендації та увагу до роботи.

Конфлікти інтересів: Автори заявляють, що не мають конфлікту інтересів.

References

Abramov, S., Krivenko, S., Roenko, A., & Lukin, V. (2013). Prediction of filtering efficiency for DCT-based image denoising. *2nd Mediterranean Conference on Embedded Computing (MECO)*. doi: 10.1109/MECO.2013.6601327.

Beauchemin, M., Thomson, K. P. B., & Edwards, G. (1996). Optimization of the Gamma-Gamma MAP filter for SAR image clutters. *International Journal of Remote Sensing*, 17(5), 1063–1067. doi: 10.1080/01431169608949067.

European Space Agency. (2016). Sentinel-1 Product Definition (S1-RS-MDA-52-7440, Ed. 2/7).

European Space Agency. (2022). Sentinel-1 Level 1 Detailed Algorithm Definition (Ed. 2.5).

Filipponi, F. (2019). Sentinel-1 GRD preprocessing workflow. *Proceedings*, 18(11). doi: 10.3390/ECRS-3-06201.

Frost, V. S., Stiles, J. A., Shanmugan, K. S., & Holtzman, J. C. (1982). A model for radar images and its application to adaptive digital filtering of multiplicative noise. *IEEE Transactions on Pattern Analysis and Machine Intelligence*, 4(2), 157–166. doi: 10.1109/TPAMI.1982.4767223.

IEEE Standard for the Deep Learning-Based Assessment of Visual Experience Based on Human Factors. (2022). IEEE Std 3333.1.3-2022. doi: 10.1109/IEEESTD.2022.9781357.

Kuan, D. T., Sawchuk, A. A., Strand, T. C., & Chavel, P. (1985). Adaptive noise smoothing filter for images with signal-dependent noise. *IEEE Transactions on Pattern Analysis and Machine Intelligence*, 7(2), 165–177. doi: 10.1109/TPAMI.1985.4767641.

Lee, J. S. (1980). Digital image enhancement and noise filtering by use of local statistics. *IEEE Transactions on Pattern Analysis and Machine Intelligence*, 2(2), 165–168. doi: 10.1109/TPAMI.1980.4766994.

Lukin, V., Abramov, S., Rubel, A., Krivenko, S., Naumenko, A., Vozel, B., Chehdi, K., Egiazarian, K., & Astola, J. (2014). An approach to prediction of signal-dependent noise removal efficiency by DCT-based filter. *Telecommunications and Radio Engineering*, 73(18), 1645–1659. doi: 10.1615/TelecomRadEng.v73.i18.40.

Medeiros, F. N. S., Mascarenhas, N. D. A., & Costa, L. F. (2003). Evaluation of speckle noise MAP filtering algorithms applied to SAR images. *International Journal of Remote Sensing*, 24(24), 5197–5218. doi: 10.1080/0143116031000115148.

Moein, F., Taban, M. R. (2024). Removing speckle noise from synthetic-aperture radar images using artificial intelligence techniques. *11th International Symposium on Telecommunications (IST)*. doi: 10.1109/IST64061.2024.10843539.

Rubel, O., Lukin, V., & de Medeiros, F. (2015). Prediction of despeckling efficiency of DCT-based filters applied to SAR images. Proc. *IEEE International Conference on Distributed Computing in Sensor Systems (DCOSS)*, 159–168. doi: 10.1109/DCOSS.2015.16.

Rubel, O., Lukin, V., Rubel, A., & Egiazarian, K. (2019). NN-based prediction of Sentinel-1 SAR image filtering efficiency. *Geosciences*, 9(7), 290. doi: 10.3390/geosciences9070290.

Rubel, O., Lukin, V., Rubel, A., & Egiazarian, K. (2020). Prediction of Lee filter performance for Sentinel-1 SAR images. *Electronic Imaging*, 2020(9), Article IQSP-371. doi: 10.2352/ISSN.2470-1173.2020.9.IQSP-371.

Rubel, O., Lukin, V., Rubel, A., & Egiazarian, K. (2021). Selection of Lee filter window size based on despeckling efficiency prediction for Sentinel SAR images. *Remote Sensing*, 13, 1887. doi: 10.3390/rs13101887.

Singh, P., Pandey, R. (2016). Speckle noise: Modelling and implementation. *International Science Press*, 9(17), 8717–8727.

Sveinsson, J. R., Benediktsson, J. A. (1996). Speckle reduction and enhancement of SAR images in the wavelet domain. *IGARSS '96. 1996 International Geoscience and Remote Sensing Symposium*, 36. doi: 10.1109/IGARSS.1996.516245.

Talebi, H., Milanfar, P. (2018). NIMA: Neural image assessment. *IEEE Transactions on Image Processing*, 27(8), 3998–4011. doi: 10.1109/TIP.2018.2831899.

Wanjiku, R. N., Nderu, L., & Kimwele, M. W. (2022). Transfer learning data adaptation using conflation of low-level textural features. *Engineering Reports*. doi: 10.1002/eng2.12603.

Wang, Z., Bovik, A. C., Sheikh, H. R., & Simoncelli, E. P. (2004). Image quality assessment: from error visibility to structural similarity. *IEEE Transactions on Image Processing*, 13(4), 600–612. doi: 10.1109/TIP.2003.819861.

Wei, S., Zhang, H., Zeng, X., Zhou, Z., Shi, J., & Zhang, X. (2022). CARNet: An effective method for SAR image interference suppression. *International Journal of Applied Earth Observation and Geoinformation*, 114, 103019. doi: 10.1016/j.jag.2022.103019.

Yu, Y., Acton, S. T. (2002). Speckle reducing anisotropic diffusion. *IEEE Transactions on Image Processing*, 11(11), 1260–1270. doi: 10.1109/TIP.2002.804276.

Zhang, L., Zhang, L., Mou, X., & Zhang, D. (2011). FSIM: A feature similarity index for image quality assessment. *IEEE Transactions on Image Processing*, 20(8), 2378–2386. doi: 10.1109/TIP.2011.2109730.

ПРОГНОЗУВАННЯ ЯКОСТІ ВІДФІЛЬТРОВАНИХ ЗОБРАЖЕНЬ З ВИКОРИСТАННЯМ ТРАНСФЕРНОГО НАВЧАННЯ НА СПЕКЛ-ШУМІ SENTINEL-1 З DENSENET-121

Р. Ж. Аль-Сенайх*, https://orcid.org/0000-0002-8059-4237

О. С. Рубель, https://orcid.org/0000-0001-6206-3988

Національний аерокосмічний університет "Харківський авіаційний інститут", вул. Вадима Манька, 17, Харків, 61000, Украина

Спекл-шум, притаманний зображенням радара із синтезованою апертурою (РСА), погіршує якість зображень та ускладнює автоматизований аналіз у застосуваннях дистанційного зондування Землі. Кількісна оцінка результатів фільтрації потребує обчислення метрик якості відносно еталонних зображень, які недоступні в операційних сценаріях РСА. У цій статті викладено метод апріорного прогнозування метрик якості відфільтрованих РСА-зображень Sentinel-1 до застосування фільтрів придушення спекл-шуму. На відміну від існуючих підходів, що прогнозують відносне покращення якості, запропонований метод прогнозує абсолютні значення п'яти метрик (PSNR, WSNR, SSIM, MS-SSIM, FSIM) для конкретного фільтра, що забезпечує пряме порівняння та раціональний вибір фільтра. Методологія використовує трансферне навчання згорткової нейронної мережі DenseNet-121, попередньо навченої на ImageNet, адаптованої для одноканальних РСА-входів шляхом архітектурних модифікацій, включаючи трансформацію вхідного шару, оптимізацію пулінгу та заміну вихідного регресійного шару. Новий конвеєр генерації синтетичних даних використовує зіставлення гістограм оптичних зображень Sentinel-2 з еталонними РСА-знімками Sentinel-1 для створення навчальних зразків із збереженням еталонних даних. Динамічне додавання гамма-розподіленого спекл-шуму зі змінним ENL $\in$ [2, 6] підвищує варіативність даних та стійкість моделі. Експерименти з шістьма класичними фільтрами (Gamma MAP, Lee, Enhanced Lee, Frost, SRAD, Kuan) демонструють високу точність прогнозування для всіх комбінацій фільтр-метрика. Коефіцієнт детермінації R^2 досягає 0,997 для найкращих комбінацій та перевищує 0,97 для більшості з 30 навчених моделей. Середні абсолютні похибки прогнозування не перевищують 0,29 дБ для PSNR та 0,014 для SSIM для всіх протестованих конфігурацій. Підхід забезпечує апріорне прогнозування якості без еталонних зображень, даючи змогу оптимізувати робочі процеси обробки РСА-даних та планування ресурсів до виконання ресурсомістких операцій фільтрації.

Ключові слова: спекл-шум, Sentinel-1, метрики якості зображень, DenseNet-121, трансферне навчання.

Рукопис статті отримано 28.10.2025
Надходження остаточної версії: 27.11.2025
Публікація статті: 30.12.2025
Received 28.10.2025
Revised 27.11.2025
Accepted 30.12.2025